J Adv Ceram

Research Article

Rapidly synthesized dense $BaTa(O,N)_3$ ceramics with high permittivity

Duan Li[1,†,✉], Sirui Ran[1,†], Jiangshan Peng[1], Lei Zeng[1], Zhiyi Yang[1], Songhe Yang[2], Yanfei Wang[1], Rongjun Liu[1]

Cite this article: Li D, Ran S, Peng J, et al. *J Adv Ceram* 2026, **15**(2): 9221223. https://doi.org/10.26599/JAC.2025.9221223

ABSTRACT: Over the past twenty years, there has been high demand for novel functional materials for use in high-capacity dielectrics. Perovskite-type oxynitrides, which are derived from the introduction of nitrogen atoms into their corresponding oxides, possess a variety of improved chemical and physical properties. The dielectric performance of $BaTa(O,N)_3$ is highly dependent on its purity, density, and microstructure. However, conventional sintering methods often result in low-density samples (< 90% theoretical density) with many impurities, leading to poor dielectric properties. In this study, we adopted a two-step sintering method, *i.e.*, rapid spark plasma sintering at a lower temperature followed by postannealing in flowing ammonia at a higher temperature, to obtain $BaTa(O,N)_3$ ceramic bulks with both high density and purity (up to 96.7% theoretical density and 97.94 wt% oxynitride phase content). The average particle size is 281.1 nm, with a uniform distribution of all the elements. The measured dielectric constant is as high as 2.1×10^5 at 100 Hz (room temperature), which surpasses the values reported for other oxynitride dielectrics. A notable and unusual dielectric enhancement was observed at elevated temperatures, with the value reaching ~10^7 at 200–250 °C. This mechanism can be attributed to defect-mediated polarization, including anion-ordering-induced permanent dipoles and oxygen vacancies, and thermally activated reconfigurable polar nanoregions that are verified by calculation and *in situ* transmission electron microscopy (TEM) analysis. These findings establish a general pathway to fabricate dense oxynitride ceramic bulks with high purity and collective permittivity for prospective applications in high-performance dielectric devices.

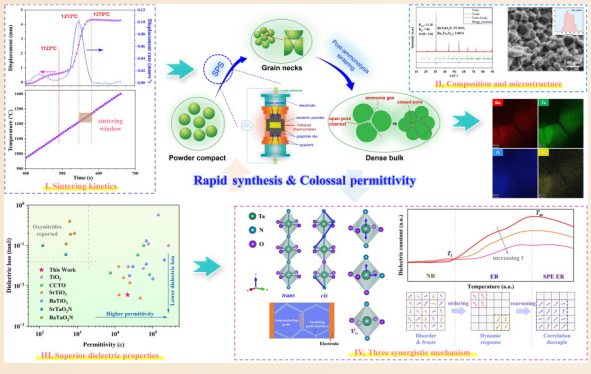

KEYWORDS: oxynitride; spark plasma sintering (SPS); densification; *in situ* transmission electron microscopy; permittivity

1 Introduction

The past twenty years have witnessed high demands for a novel functional material family – perovskite-type oxynitrides [1–3]. Compared with the corresponding oxides, the introduction of nitrogen (with a lower electronegativity than that of oxygen) into the lattice enhances the chemical and physical properties of the material. In particular, tantalum oxynitrides with the formula $ATa(O,N)_3$ (A = Ca, Sr, Ba, Eu, La, Ce, Pr, etc.) have attracted considerable attention because of their distinctive optical, dielectric and photocatalytic properties [2,4–6]. It has been reported that $BaTa(O,N)_3$ oxynitride possesses a large permittivity (> 5000) [2], making it a highly promising candidate for applications in modern electronics, sensors, energy storage systems, and multifunctional devices [7]. In addition, tantalum oxide perovskites exhibit good thermal stability and chemical corrosion resistance in harsh environments [6]. These unlocking features enable their wide application in high-capacity dielectrics [6,8–14] as well as next-generation visible light-driven photocatalysts [4,5,15–18] for renewable hydrogen energy.

The preparation of tantalum oxide powder with controlled stoichiometry, uniformity and fine particle size is crucial for making high-performance ceramics. Ammonolysis of a complex oxide precursor or a mixture of metal salts under a flowing NH_3 atmosphere is a typical method that usually consumes tens of hours to obtain oxynitrides with the desired purity [1–3]. Recently, we developed a novel approach by rapidly heating metal oxide precursors with urea inside a pressureless spark plasma

† Duan Li and Sirui Ran contributed equally to this work.

[1] Science and Technology on Advanced Ceramic Fibers and Composites Laboratory, College of Aerospace Science and Engineering, National University of Defense Technology, Changsha 410073, China. [2] Key Laboratory of Interfacial Science and Engineering of Materials (SKLISEM), School of Environmental Science and Engineering, Southern University of Science and Technology, Shenzhen 518055, China.

✉ Corresponding author. E-mail: duan_li_2016@163.com

Received: September 17, 2025; Revised: November 13, 2025; Accepted: November 28, 2025

sintering setup to achieve an oxynitride powder with > 97 wt% purity within minutes. Furthermore, the consolidation of such oxynitride powder to form ceramic bulks is not only important for performance evaluation but also necessary for device fabrication [10,14]. Previous studies have revealed that perovskite-type oxynitrides are difficult to sinter, as the sufficient densification temperatures required always exceed their thermal dissociation temperatures [2,3]. On this basis, conventional sintering methods, which are usually conducted at elevated temperatures for longer dwell times, can lead to full or partial decomposition of the oxynitrides [10]. An alternative method involves the use of sintering additives or high external pressure, which can accelerate the densification process [8–12]. Hosono *et al.* [8,9] fabricated $BaTaO_2N$ bulks by adding 2.5 wt% $BaCO_3$ as an additive and applying postammonolysis, and the resulting relative density reached 92.6% for phase-pure $BaTaO_2N_{0.85}$. They also employed hot isostatic pressing equipment for densifying $SrTaO_2N$ at 190 MPa in a nitrogen atmosphere to obtain pure $SrTaO_2N_{0.7}$ pellets with a relative density value of 88.6%. Y.R. Zhang *et al.* [19,20] reported that both $SrCO_3$ and La_2O_3 were effective at achieving single-phase $SrTaO_2N$ bulks with relative densities higher than 90% and that anion vacancies can be eliminated by postannealing in flowing ammonia. However, achieving both high purity (> 97 wt% perovskite phase) and high density (> 95% theoretical density) is still a challenge for these oxynitride ceramics. The reason is that only the surface region of the sintered oxynitrides can be recovered by postammonolysis, whereas the inner part is filled with isolated closed pores that prevent the entrance of gaseous ammonia.

Spark plasma sintering (SPS) [21] is a fast sintering technique that involves Joule heating and electric field effects. The densification of these perovskite-type oxynitrides through SPS has shown good merits over conventional sintering approaches [22–24]. However, it is still difficult to obtain oxynitrides with both high purity and high density merely by SPS. On the other hand, previous investigations have revealed that the physical properties of tantalum oxynitrides are strongly influenced by structural distortions (e.g., $Ta(O,N)_6$ octahedra tilting) that may arise from A site cation displacements, the arrangement of anion atoms and anionic nonstoichiometry [25–28]. Modifications of anionic characteristics such as the ratio, order and deficiency add new dimensions to tune the electronic and dielectric behavior of materials, which are less explored.

In the present work, we attempted to fabricate $BaTa(O,N)_3$ ceramic bulks with the desired density and purity by employing a two-step sintering strategy combining high-pressure SPS and postammonolysis. SPS processing was conducted to rapidly obtain oxynitride bulks with high open porosities. The subsequent postammonolysis sintering could contribute to compositional recovery as well as further densification. During sintering processes, the local structure of oxynitrides can be tailored, and extrinsic defects (pores/impurities) can be eliminated to obtain a colossal permittivity that has been underestimated by past research. To the best of our knowledge, this is the first report on the rapid consolidation of $BaTa(O,N)_3$ monoliths with simultaneously dense structures, high purities and superior dielectric constants.

2 Materials and methods

2.1 Preparation

$BaTaO_2N$ powder with a high purity (oxynitride phase content > 99 wt%) was used as a sintering precursor. The powder was self-synthesized by calcining a mixture of $BaCO_3$, Ta_2O_5 and urea according to our previous work [6]. SPS processing of $BaTaO_2N$ was performed via spark plasma sintering (SPS-3.20 mkII, Sumitomo Coal Mining, Japan) under pressure conditions. During a standard SPS process, a batch of ~1 g $BaTaO_2N$ powder was prepressed and loaded into a cylindrical graphite die with an inner diameter of 10 mm. The temperature was automatically raised to 600 °C over a period of 3 min. Afterwards, it was monitored by a radiation pyrometer focused on the surface of the die, and a uniaxial mechanical pressure of 0–100 MPa was applied and held constant until the end of heating. To analyze the sintering kinetics, the shrinkage and linear shrinkage rates of the sample along the longitudinal direction were simultaneously recorded at 50 MPa and 100 °C/min. For all the SPS procedures, the samples were sintered under a 0.7 atm N_2 atmosphere and naturally cooled to room temperature after heating. The sintering parameters were optimized, and the obtained samples were collected and polished (to remove surface contamination) for further ammonolysis sintering (Table 1). Postammonolysis sintering was carried out in a tube furnace under flowing ammonia conditions. The SPSed pellets were placed inside the alumina boat. The samples were heated to 1300 °C at a heating rate of 10 °C/min. Various dwell times (30–480 min) were investigated to produce oxynitride bulks with different compositions. After heating, all the samples were naturally cooled to room temperature and collected for characterization.

2.2 Characterizations

The phase purity of the oxynitride powder precursor and sintered bulk samples was examined via X-ray diffraction (XRD; D8 Advance, Bruker Axs Co., Germany) via Cu Kα radiation over a 2θ range of 10°–90°. XRD profile fitting and calculations of the oxynitride phase contents were performed via the Rietveld software package (TOPAS 4.2) in fine scan mode. The bonding structure of the oxynitrides was evaluated via X-ray photoelectron spectroscopy (XPS; Thermo ESCALAB 250XI, Thermo Fisher Scientific Co., USA) with AlKα excitation. The O/N ratio was determined through semiquantitative XPS analysis. *In situ* XRD measurements of the sintered oxynitride ceramics were performed on a Rigaku SmartLab diffractometer equipped with a high-temperature reaction chamber (Anton Paar HTK 1200 N). The samples were heated from 25 to 300 °C under a nitrogen atmosphere at a ramp rate of 5 °C/min. Diffraction patterns were continuously recorded in the 2θ range of 10°–90° with a step size of 0.02° and a scanning speed of 2 (°)/min using Cu Kα radiation (λ = 1.5406 Å). The morphology of the oxynitride samples was investigated via a scanning electron microscope (SEM; MIRA3,

Table 1 Sintering parameters, density, grain size, and composition of the obtained oxynitride bulks

Sample	Preparation parameter				Relative density (%)	Grain size (nm)	Oxynitride phase content (wt%)	O/N (at%)
	Heating rate (°C/min)	Temperature (°C)	Dwell time (min)	Mechanical pressure (MPa)				
BTON-P	300	1000	1	0	—	213.9±76.6	99.39	2.20
BTON-SPS	300	1250	1	100	94.9	237.6±77.5	95.83	1.85
BTON-SPS-AM	10	1300	480	0	96.7	281.1±86.6	97.94	2.08

Tescan Ltd., Czech Republic) and a transmission electron microscope (TEM; Technai G2 F20 S-TWIN 200kV, FEI Co., USA) equipped with an energy-dispersive spectroscopy (EDS) detector. EDS mapping of Ba/Ta/O/N was conducted in HAADF-STEM mode, and the contents of Ba/Ta were quantitatively evaluated. *In situ* TEM heating experiments were performed via a JEOL JEM-2100F microscope equipped with a Gatan heating holder (model 628). The sample was heated from room temperature to 300 °C at a ramp rate of 10 °C/min in a high-vacuum environment (< 10^{-5} Pa). Real-time HRTEM images were recorded at different temperature intervals to monitor the microstructure evolution. Selected area fast Fourier transform (FFT) analyses were conducted on the acquired HRTEM images via the Gatan digital micrograph software. The FFT patterns were obtained from regions of interest. To minimize electron beam-induced artifacts, the beam current was maintained below 1 nA during acquisition. The grain size of the sintered samples was evaluated on the basis of SEM images via the linear intercept method with a three-dimensional correction factor of 1.2. For each sample, at least 200 grains were measured to obtain the average value and standard deviation. The thermal stability of the oxynitride was examined by a thermal gravimetric and differential scanning calorimetry device (TG-DSC; DSC204F1, Netzsch, Germany) under N_2, with a heating rate of 10 °C/min from room temperature to 1300 °C. The density, porosity and open porosity of the oxynitride bulk materials were measured via water penetration and Archimedes' method, with a value of 8.743 g/cm^3 assumed to be the theoretical density of the fully dense $BaTa(O,N)_3$ bulk material. More than three values were obtained for averaging. The pore size and pore size distribution of the sintered samples were measured via a mercury intrusion porosimeter (Micromeritics AutoPore IV 9500, Norcross, Georgia, USA). The surface tension, contact angle and density of the mercury were set to 0.485 N/m, 130° and 13.5364 g/cm^3, respectively. The dielectric behavior in terms of relative permittivity, dielectric loss and impedance was measured via a dielectric spectrum measurement system (VDMS-2000, Partulab, China) with a impedance analyzer (WK6500, Wayne kerr, China) over the frequency range from 10^2–10^6 Hz at a temperature range of RT–300 °C. To form the electrode contacts, the oxynitride pellet was covered by Ag-pasted electrodes on both sides.

2.3 Calculation

First principles calculations were performed via projector augmented wave (PAW) pseudopotentials with exchange and correlation in the Perdew–Burke–Ernzerhof (PBE) formalism of density function theory (DFT) as implemented in the Vienna *ab initio* simulation package (VASP). The valence atomic configurations are $5s^25p^66s^2$ for Ba, $5d^36s^2$ for Ta, $2s^22p^4$ for O, and $2s^22p^3$ for N. Geometry optimizations were performed before single-point energy calculations, and the self-consistent convergence accuracy was set at 1×10^{-5} eV/atom. The convergence criterion for the maximal force on atoms is 0.02 eV/Å. The cutoff energy of the plane wave function is set to 500 eV. A 4 × 4 × 4 Monkhorst–Pack grid is chosen for sampling the Brillouin zones (BZs). The Heyd–Scuseria–Ernzerhof (HSE06) method was used for band calculation.

3 Results and discussion

3.1 Analysis of the sintering kinetics and mechanism for $BaTa(O,N)_3$

Understanding the sintering behavior of $BaTa(O,N)_3$ ceramics is critical for developing a densification strategy, before which the thermal stability of the oxynitride deserves investigation. Figure 1(a) shows the TG-DSC curves of the as-received $BaTa(O,N)_3$ powder tested in a nitrogen atmosphere. The oxynitride compound clearly decomposes from the beginning to 1300 °C, which can be divided into two stages, i.e., removal of adsorbed water or residual moisture (stage I, RT–605 °C) and dissociation into nitrides/oxides/oxynitride species (stage II, 605–1300 °C). Notably, the two exothermic peaks (810 and 1220 °C) displayed in the DSC curve during the entire process seem to indicate the complex dissociation processes of $BaTa(O,N)_3$. Moreover, the sintering kinetics of the oxynitride were evaluated according to the recorded longitudinal shrinkage displacement and displacement rate curves, as shown in Fig. 1(b). A positive and increasing shrinkage rate appears when the heating temperature reaches 1123 °C, indicating the beginning of the densification process. The shrinkage displacement rate reached a maximum at 1213 °C, which implies that the macroscopic diffusion rate was the highest and that grain growth took place rapidly afterwards. It can also be observed that shrinkage begins to remain stable at 1270 °C, suggesting the end of densification. The 'kinetic window' for sufficient densification (better density) but with suppressed grain growth (fine grain structure) is then deduced to be 1120–1270 °C. Moreover, considering that the oxynitride family is prone to decompose at high temperatures from a thermodynamic point of view, the optimal sintering temperature applied should be moderate to ensure both the desired densification and minimized decomposition. On the other hand, the heating rate determines the total sintering time and needs to be optimized. A lower heating rate means a longer exposure time at high temperature, whereas a higher heating rate will produce greater thermal stress and even cracks in the sintered sample.

According to classical solid-state sintering theory [29,30], grain necks are formed during the initial stage, whereas the intermediate sintering stage involves neck growth and compact shrinkage. At this stage, the open pore network is generated, followed by the final sintering stage, in which closed pores are generated. Thus, to obtain a sintered bulk with good density and open porosity to ensure sufficient postammonolysis sintering, sintering should be controlled at the 'critical point' between the intermediate and final stages (Fig. 1(c)). To determine this point, we sintered samples with different regimes (all with 50 MPa mechanical pressure, 1 min dwell and different temperatures) at the end of the second sintering stage and then calculated the relative density with respect to the open porosity ratio (open porosity divided by the total porosity percentage). Three factors need to be considered: higher sintered density, higher open porosity ratio and lower sintering temperature. As shown in Fig. 1(d), the red circles indicate the proper sintering temperature ranges for considering each factor. Therefore, the optimal sintering temperature is 1250 °C, with 87.8% TD and a 49.1% open porosity ratio. As shown by the mercury porosimetry results (Fig. 1(e)), the pore size of the sample sintered at 1250 °C was unimodal, with an average pore diameter of 252.9 nm. The SEM image of the cross-section of the ceramic (Fig. 1(f)) also reveals a porous structure and a fine gain size of 50–200 nm. This pore structure is beneficial for ammonia gas penetration during subsequent postammonolysis sintering.

3.2 Composition and microstructure of the sintered $BaTa(O,N)_3$ ceramics

The composition and microstructure of the oxynitride powder and sintered samples were studied via a series of measurements,

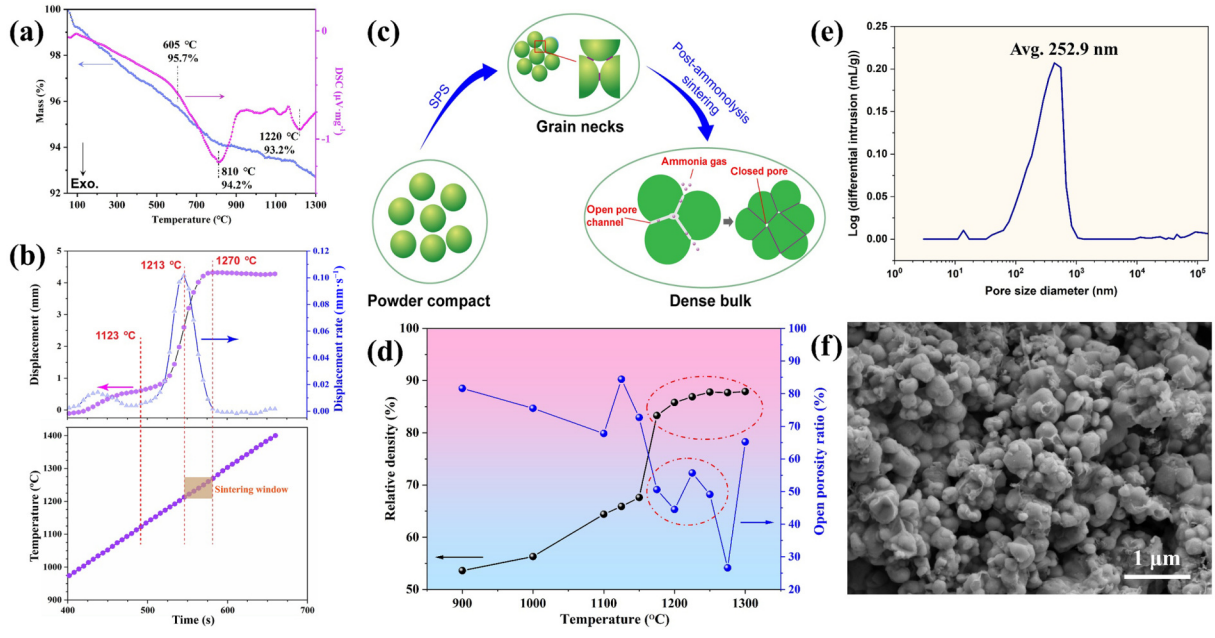

Fig. 1 Analysis of the sintering kinetics and mechanism for $BaTa(O,N)_3$: (a) TG-DSC curves of the as-received $BaTa(O,N)_3$ powder tested in a nitrogen atmosphere, (b) recorded longitudinal shrinkage displacement and displacement rate curves during a standard sintering procedure (50 MPa, 100 °C/min), (c) schematic diagram revealing the 'critical point' control during two-step sintering, (d) variations in the relative density and open porosity ratio with sintering temperature (50 MPa, 100 °C/min), (e) pore size distribution of the sample sintered at 1250 °C and (f) SEM image of the cross-section of the sample sintered at 1250 °C.

including X-ray diffraction (XRD), X-ray photoelectron spectroscopy (XPS), scanning electron microscopy (SEM) and transmission electron microscopy (TEM). Figure 2 shows the composition and structure of $BaTa(O,N)_3$ before and after sintering. The XRD patterns listed in Figs. 2(a)–2(c) represent the synthesized powder (BTON-P), SPSed ceramic bulk (BTON-SPS) and ammonolysis-treated bulk (BTON-SPS-AM), respectively, as shown in Table 1. Notably, all the samples presented standard diffraction peaks corresponding to the oxynitride phases (*Pm*3(_)*m*, ICSD_#62619). The existence of the corresponding oxides ($Ba_5Ta_4O_{15}$, *P*4/*mbm*, ICSD_#16028) was also detected, and the low peak intensity revealed a minor concentration. The Rietveld refinement results confirmed the coexistence of 99.39 wt% $BaTaO_2N$ and 0.61 wt% $Ba_5Ta_4O_{15}$ for BTON-P, 95.83 wt% $BaTaO_2N$ and 4.17 wt% $Ba_5Ta_4O_{15}$ for BTON-SPS, and 97.94 wt% $BaTaO_2N$ and 2.06 wt% $Ba_5Ta_4O_{15}$ for BTON-SPS-AM. This finding shows that SPS treatment at high temperatures and pressures can improve the density of the oxynitride ceramics but also reduce their purity. The subsequent ammonolysis sintering can improve the density and purity.

The XPS spectra of the sintered $BaTa(O,N)_3$ ceramics are shown in Figs. 2(d)–2(h). Figure 2(d) shows the XPS wide-scan spectrum of the $BaTa(O,N)_3$ ceramics prepared via the optimized process. Five characteristic peaks of Ta 4f, N 1s, O 1s, and Ba 3d appear in Fig. 2, indicating the element composition of the compound, and the presence of C is caused mainly by the sample processing and testing environment. The main peaks of Ba 3d, Ta 4f, N 1s, and O 1s are processed by peak segmentation according to the key information queried in the NIST database. The high-resolution Ba 3d spectrum in Fig. 2(e) reveals two distinct peaks, characteristic of spin-orbit coupling in the Ba 3d orbital, with a spin-orbital splitting energy consistent with the database values. Similarly, the Ta 4f spectrum (Fig. 2(f)) exhibits significant spin-orbit coupling, resulting in its splitting into two diagnostic peaks: Ta $4f_{7/2}$ (binding energy of 25.37 eV) and Ta $4f_{5/2}$ (binding energy of 27.28 eV), confirming the existence of pentavalent tantalum (Ta^{5+}). The N 1s (Fig. 2(g)) and O 1s (Fig. 2(h)) data demonstrate that lattice nitrogen and lattice oxygen exhibit characteristic peaks at 396.02 and 529.35 eV, respectively, indicating the coexistence of Ta–O and Ta–N bonds in $BaTa(O,N)_3$. Notably, a significantly reduced lattice nitrogen content is observed, which is attributable to surface nitrogen loss/oxidation phenomena during high-temperature sintering, which transforms partial nitrogen into oxidized nitrogen species (401.25 eV) or adsorbed nitrogen-containing compounds (403.70 eV). Comparative analysis via supplementary O 1s data from powder samples (Fig. 2(i)) revealed a consistent subpeak at 530.79 eV in both the bulk and powder samples, which was typically assigned to the characteristic oxygen vacancy peak [31]. Given that nitrogen substitution for lattice oxygen sites intrinsically promotes oxygen vacancy formation in oxynitrides and that the densification process further elevates oxygen vacancy concentrations in bulk materials, these findings align with those of semiquantitative XPS analysis (V_O/O_L, the ratio of oxygen vacancies to lattice oxygen).

The electron microscopy analysis in Fig. 3 provides comprehensive insights into the microstructural evolution and phase composition of $BaTa(O,N)_3$ synthesized via distinct processing routes. The morphological progression revealed by SEM (Figs. 3(a)–3(c)) highlights a critical transition from irregular, agglomerated powder nanoparticles in BTON-P (mean diameter: 213.9±76.6 nm) to highly uniform and faceted grains after SPS, with an average grain size of 237.6±77.5 nm. With ammonolysis sintering, the sample experienced minor grain growth to 281.1±86.6 nm, highlighting the role of postannealing sintering in reducing porosity and improving densification. This progressive particle refinement and narrowing size distribution signifies enhanced sintering control through advanced processing techniques, which directly correlates with improved grain boundary engineering and densification behavior essential for functional ceramics. High-resolution structural analysis (Figs. 3(g)–3(j)) confirmed the exceptional crystallinity of the BTON-SPS-AM material. The distinct lattice fringes at 2.990 Å (corresponding to the $(01\bar{1})$ planes) and 2.303 Å (corresponding to the (111)

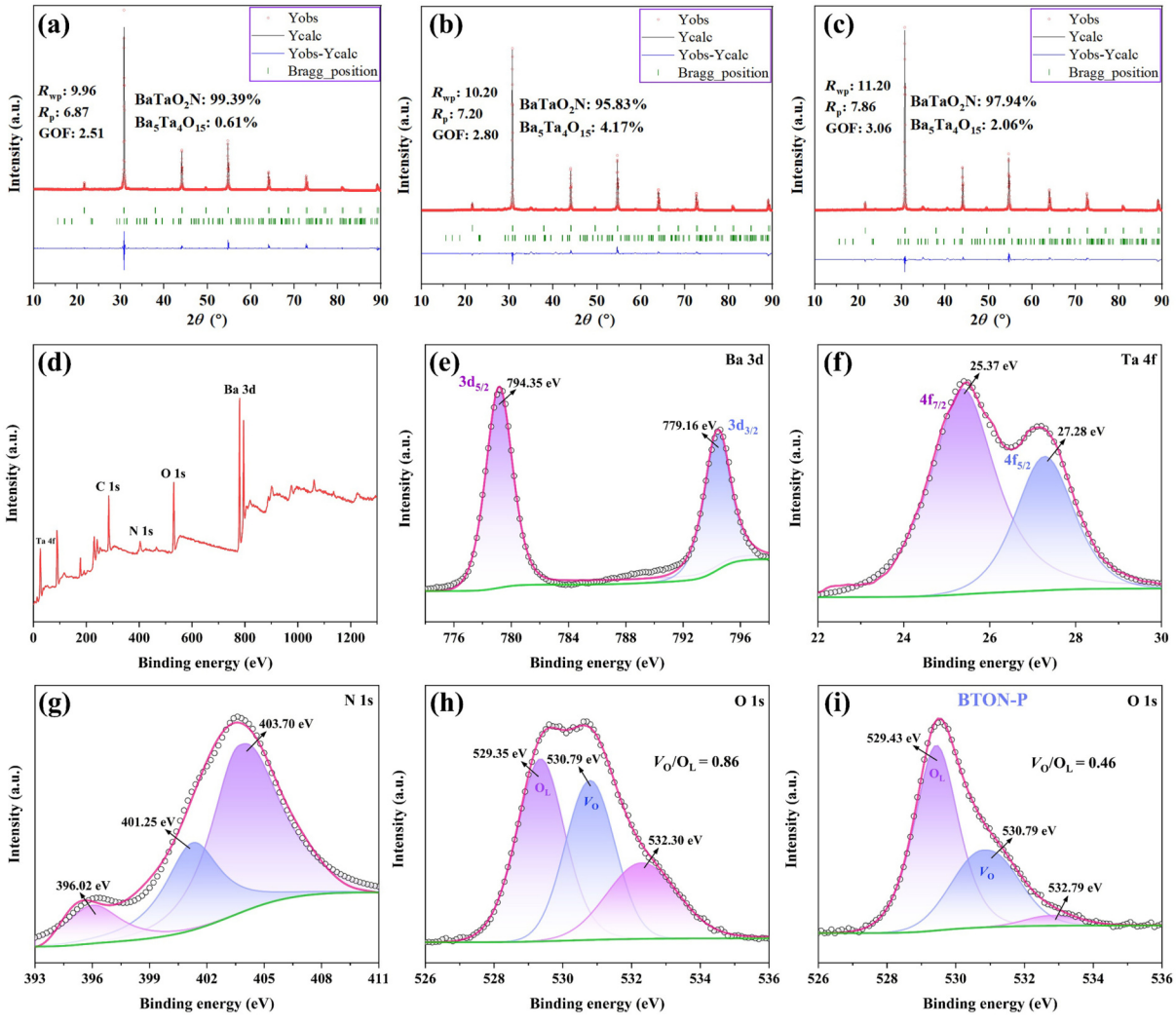

Fig. 2 Compositions of $BaTa(O,N)_3$: (a) BTON-P, (b) BTON-SPS and (c) BTON-SPS-AM. XPS spectra of BTON-SPS-AM: (d) wide scanning spectrum, (e) Ba 3d, (f) Ta 4f, (g) N 1s, (h) O 1s. (i) Supplementary XPS O 1sspectrum of BTON-P.

planes) can be indexed to the $[2\bar{1}\bar{1}]$ zone axis. Coupled with the single-crystalline diffraction pattern in the fast Fourier transform (FFT), the data validate the formation of phase-pure perovskite. These metrics align precisely with the theoretical lattice parameters for cubic $BaTaO_2N$, indicating minimal structural defects and crystallographic integrity. Most critically, the STEM-HAADF map in Fig. 3(k) provides compelling evidence of compositional homogeneity. The uniform spatial distributions of Ba (red), Ta (cyan), O (green), and N (magenta) throughout the sintered grains at sub50 nm resolution confirm the absence of deleterious elemental segregation or secondary phases. This chemical homogeneity, which is particularly challenging to achieve in multianionic oxynitride systems, is important for optimizing the chemical stability and dielectric properties of the oxynitride.

3.3 Colossal permittivity and mechanism for $BaTa(O,N)_3$

The dielectric properties of the synthesized oxynitride were characterized by the relative dielectric constant (ε_r) and dielectric loss (tanδ). Figure 4(a) shows the dielectric curve of BTON-SPS-AM at a frequency of 100 Hz–1 MHz at 25 °C. The $BaTa(O,N)_3$ ceramics have a high dielectric constant and a low dielectric loss below 1000 Hz, whose dielectric loss is less than 0.01 and whose dielectric constant is as high as 2.1×10^5. Within the whole measured frequency range, the dielectric constant of the $BaTa(O,N)_3$ ceramics remains above 10,000, whereas the dielectric loss is relatively high in the higher frequency range. At 1 MHz, the tanδ value increases significantly to 1.64. To explain this phenomenon, the conductivity of the samples was measured, and the average value was 1.076×10^{-5} s·cm^{-1} (25 °C). Thus, high dielectric loss in the higher frequency range can be attributed to anionic defects caused by conductivity in the crystal and nitrogen loss. As demonstrated in Fig. 4(b), $BaTa(O,N)_3$ ceramics exhibit an unprecedented dielectric constant exceeding 20 million at 100 Hz/235 °C, significantly surpassing all previously reported dielectric systems. As the temperature increases, the peak shifts toward higher frequencies, indicating a distinct thermally activated process and typical Debye relaxation behavior. To investigate the underlying mechanism responsible for this relaxation, we employed the Vogel-Fulcher empirical formula [32], through which the freezing temperature (T_f) was estimated to be 125 °C.

The impedance spectrum (Fig. 4(c)) of BTON-SPS-AM exhibited a single, continuously varying semicircle within the tested temperature range, indicating that the grain boundary resistance (R_{gb}) was significantly greater than the grain resistance (R_g) and thus dominated the impedance response. The diameter of this semicircle decreases significantly with increasing temperature, which is closely associated with an increase in the concentration and mobility of thermally activated charge carriers. The pronounced deviation of the semicircle's center from the real

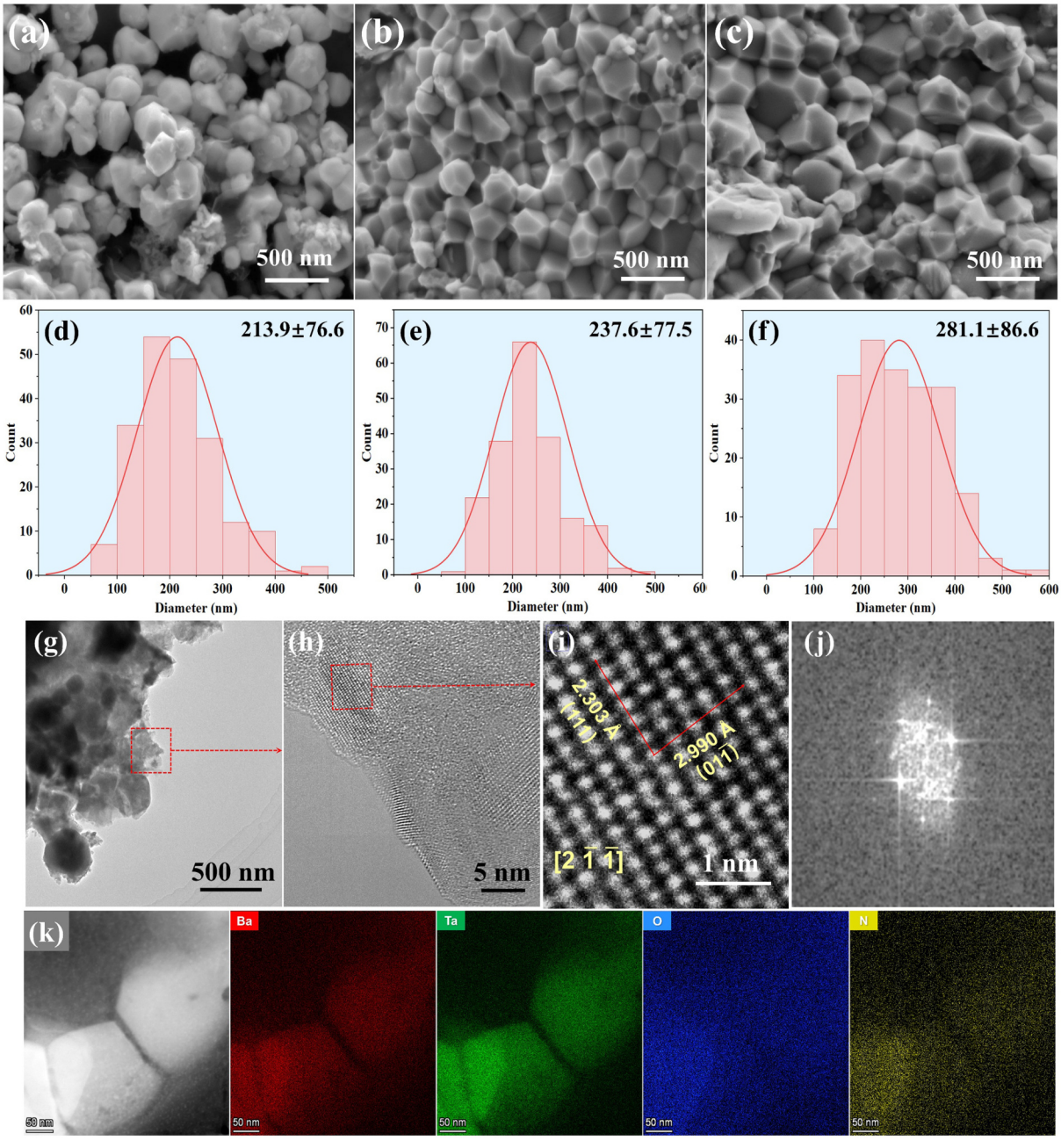

Fig. 3 Electron microscopic characterization of $BaTa(O,N)_3$: SEM images showing the morphology of (a) BTON-P, (b) BTON-SPS, and (c) BTON-SPS-AM; particle size distribution histograms corresponding to SEM images of (d) BTON-P, (e) BTON-SPS, and (f) BTON-SPS-AM; (g) low-resolution and (h–i) high-resolution TEM image of BTON-SPS-AM displaying the [2$\bar{1}\bar{1}$] zone; (j) FFT of the lattice; (k) STEM-HAADF image of the sintered grains and mapping of the distribution of Ba/Ta/O/N elements.

axis (Z') confirms that the relaxation behavior is of a nonideal Debye type. Therefore, a constant phase element (CPE) was introduced into the equivalent circuit to accurately describe this nonideal dielectric response. The absence of distinct, separated semicircles corresponding to grains and grain boundaries suggests that their relaxation times are very similar, resulting in overlapping responses within the measured frequency range and collectively contributing to the observed single impedance arc. The contraction of this arc directly reflects the decrease in the overall resistance of the material with increasing temperature, which is characteristic of a typical thermally activated conduction process [33,34].

The comparative analysis in Fig. 4(d) confirms that our oxynitride delivers a room-temperature colossal permittivity comparable to mainstream dielectrics and low dielectric loss (tanδ < 0.01) [8–13,22,33–52]. The oxynitride we synthesized has a giant dielectric constant no less than that of mainstream dielectric materials and low loss. Crucially, this material outperforms conventionally synthesized oxynitrides by 1–2 orders of magnitude in permittivity and an ~10-fold reduction in dielectric loss. Furthermore, the observed high-temperature dielectric properties, coupled with the excellent physicochemical characteristics (thermal stability and chemical corrosion resistance) identified in previous studies [6], underscore the long-term service stability of this functional ceramic under extreme conditions.

To explain the very unusual high-temperature dielectric performance, we conducted *in situ* high-temperature XRD and

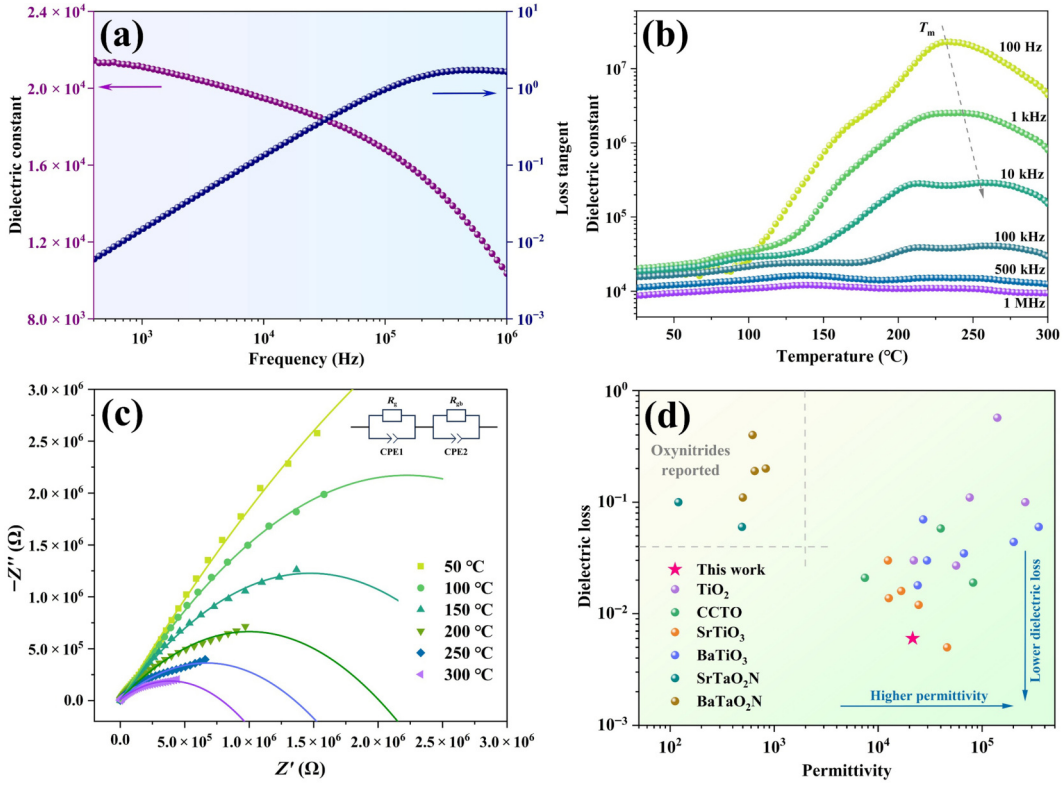

Fig. 4 Dielectric properties of BTON-SPS-AM: (a) relative dielectric constant and dielectric loss values varying with frequency, (b) temperature-dependent dielectric constant values with varying frequency, (c) complex impedance spectra and (d) comparison of dielectric properties with those of previously reported dielectric materials.

TEM analyses. XRD patterns collected from 25 to 300 °C (Fig. 5(a)) reveal invariant peak positions and intensities, ruling out conventional ferroelectric phase transitions. Atomic-resolution TEM images (Fig. 5(b)) reveal that the as-synthesized $BaTa(O,N)_3$ consists of defective nanocrystalline clusters at room temperature, as evidenced by diffuse Debye rings in the FFT insets, indicating short-range order but long-range structural disorder (within a scale of ~30 nm). Upon heating, the progressive annealing of edge defects in nanoclusters (100–150 °C) prompts their coalescence, ultimately resulting in the formation of a nearly single-crystal morphology at 200 °C, which is characterized by the disappearance of diffuse Debye rings and the emergence of distinct diffraction spots. These coalesced nanoclusters, defined as polar nanoregions (PNRs) [53–55], evolve into an optimal size of ~5 nm at 225 °C, which coincides with the peak permittivity (Fig. 4(b)) through a dynamic matching mechanism between the dipole response and domain size. Beyond this temperature, PNR coarsening (10–20 nm at 250 °C) and eventual long-range ordering (300 °C) decouple dipole correlations, leading to attenuation of the permittivity. This thermal evolution is consistent with dipole glass (DG) [56,57] behavior in compositionally disordered perovskites. Spatially heterogeneous PNRs undergo dynamic freezing below freezing temperature (T_f) (a nonergodic state with history-dependent properties) while exhibiting ergodic behavior above T_f where dipoles dynamically reorient. In summary, *in situ* XRD and TEM collectively demonstrate that the colossal permittivity originates from defect-mediated PNR reorganization within a structurally stable lattice rather than from conventional ferroelectric phase transitions.

The bandgap of $BaTaO_2N$ was estimated to be 1.77 eV by applying the Kubelka–Munk (K–M) method to UV–Vis diffuse reflectance spectroscopy (Fig. 6(a)), which is consistent with DFT calculations (Figs. 6(b) and 6(c)). This narrow band gap confirms the presence of semiconducting grains in $BaTa(O,N)_3$. Combined with the impedance analysis (Fig. 4(c)), which reveals that R_{gb} is significantly larger than R_g, it can be reasonably concluded that the interface barrier layer capacitance [7] (IBLC) effect serves as a key mechanism contributing to the observed colossal permittivity of $BaTa(O,N)_3$. The density of states (DOS) plot reveals significant Ta-5d/O-2p orbital hybridization near the Fermi level. Furthermore, the introduction of nitrogen via N/O substitution leads to the formation of oxygen vacancies [58], which generate localized electronic states. These electronic states not only enhance electronic correlations but also promote ionic displacement polarization [59,60]. As shown in Fig. 6(d), $BaTa(O,N)_3$ exhibited a distinct thermally activated dielectric relaxation. To elucidate the underlying mechanism of this relaxation, we applied the thermally activated polaron hopping model [61–63], derived from the Debye equation. This relaxation process follows the Arrhenius law, which can be described by Eq. (1):

$$T\varepsilon''_{\max} = \frac{N_0\mu^2}{3k_B}\exp\left(-E_A/(k_BT)\right) \quad (1)$$

where $\varepsilon''_{\max}$ represents the peak of dielectric loss, N_0 represents the density of hopping polarons per unit volume, μ represents the hopping dipole moment, k_B is the Boltzmann constant, and E_A is the activation energy. The slope change in the Arrhenius-fitted curve ($\ln(\varepsilon''_{\max}T)$ vs. $1/T$, Fig. 6(d)) indicates the coexistence of two different thermally activated polarization mechanisms: at low temperatures, frozen polarons permit only interfacial polarization (E_A = 0.092 eV), whereas at high temperatures, activated polaron hopping coexists with interfacial effects (E_A = 0.324 eV). The fitting results are basically consistent with the high-temperature dielectric properties observed in Fig. 4(b).

As depicted in Fig. 7, three synergistic mechanisms underlie the collective permittivity: (i) Interface barrier layer capacitance

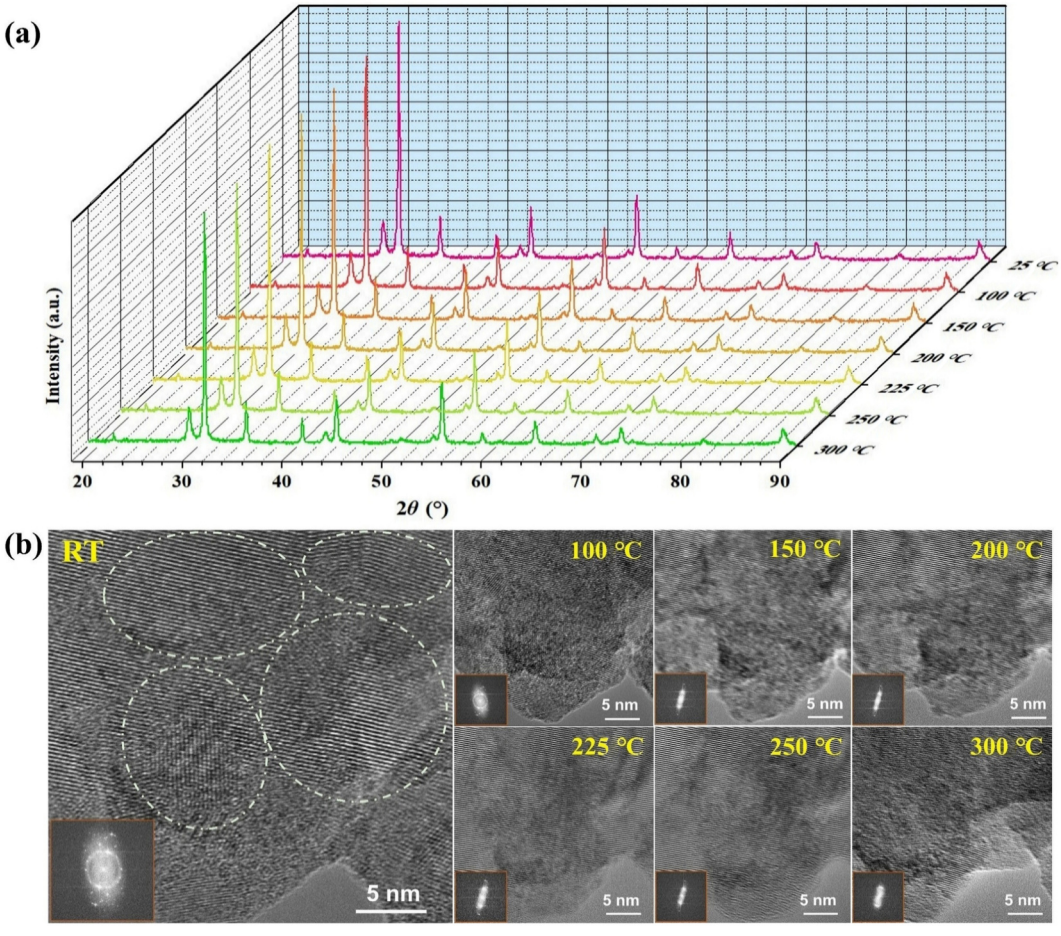

Fig. 5 (a) *In situ* XRD patterns and (b) TEM images (the insets in the lower left corner are the FFT images) of BTON-SPS-AM collected from 25 to 300 °C.

(IBLC), where carrier accumulation at interfaces between semiconducting grains and insulating grain boundaries forms nanoscale capacitive networks [7,64]; (ii) Defect-mediated polarization, involving both permanent local dipoles generated by *cis*/*trans* BO_4N_2 configurations (N adjacent/opposite) that break octahedral symmetry [26,27] and defect dipole polarization associated with oxygen vacancies [34,65], as illustrated in Fig. 7(a); (iii) thermally activated hopping polarization, involving both the thermal excitation of polarons and the subsequent formation of dynamically reconfigurable polar nanoregions (PNRs) during structural ordering—these two mechanisms that act synergistically to enhance the dielectric response [52,59]. Defect-mediated colossal permittivity is characterized by the freezing temperature (T_f), which serves as a key thermodynamic indicator of defect dipole behavior [36,66].

The notable increase in the permittivity at elevated temperatures (Fig. 4(b)) can be attributed to the increased activation energy of $BaTa(O,N)_3$ observed under high-temperature conditions, as depicted in Fig. 6(d). This activation energy is strongly dependent on both the concentration and type of defects [61]. Owing to their richer defect diversity, our oxynitrides exhibit a more pronounced increase in permittivity when the temperature exceeds T_f. The underlying microscopic mechanism of this unique thermally activated dielectric relaxation is further illustrated in Fig. 7(b), where three distinct temperature zones are identified, corresponding to the polarization responses of the nonergodic relaxor NR, ergodic relaxor ER, and superparaelectric (SPE) ER [56,57]. Below T_f, the defect dipoles remain frozen, and long-range disordered NRs exhibit only a weak response to external electric fields. As the temperature exceeds T_f, the dipoles become mobile, allowing the thermally activated ER to respond dynamically to the field and leading to a substantial increase in permittivity. However, beyond the peak temperature (T_m), PNR coarsening triggers the decoupling of dipole correlations, resulting in a subsequent attenuation of the permittivity.

Critically, while perovskite oxynitrides exhibit intrinsically colossal permittivity, conventional synthesis methods fail to produce ceramics with simultaneous high purity (> 97%) and density (> 95% TD). This performance limitation stems from extrinsic defects—including impurity phases and open pores (> 10 vol%)—which suppress intrinsic polarization and reduce effective permittivity through interfacial charge scattering. Furthermore, these microstructural imperfections decouple atomic-scale dipole correlations from the macroscopic dielectric response, thereby disrupting the structure–property relationship essential for achieving theoretical performance. Our rapid sintering process overcomes these limitations by crafting a defect-engineered microstructure that simultaneously achieves exceptional density and phase purity. Within this optimized structure, precisely controlled oxygen vacancies activate dipole reconfiguration [29,65], thereby eliminating extrinsic effects and enabling the full manifestation of the intrinsic collective permittivity.

4 Conclusions

In summary, this work successfully demonstrated a novel two-step processing route for fabricating dense, high-purity $BaTa(O,N)_3$

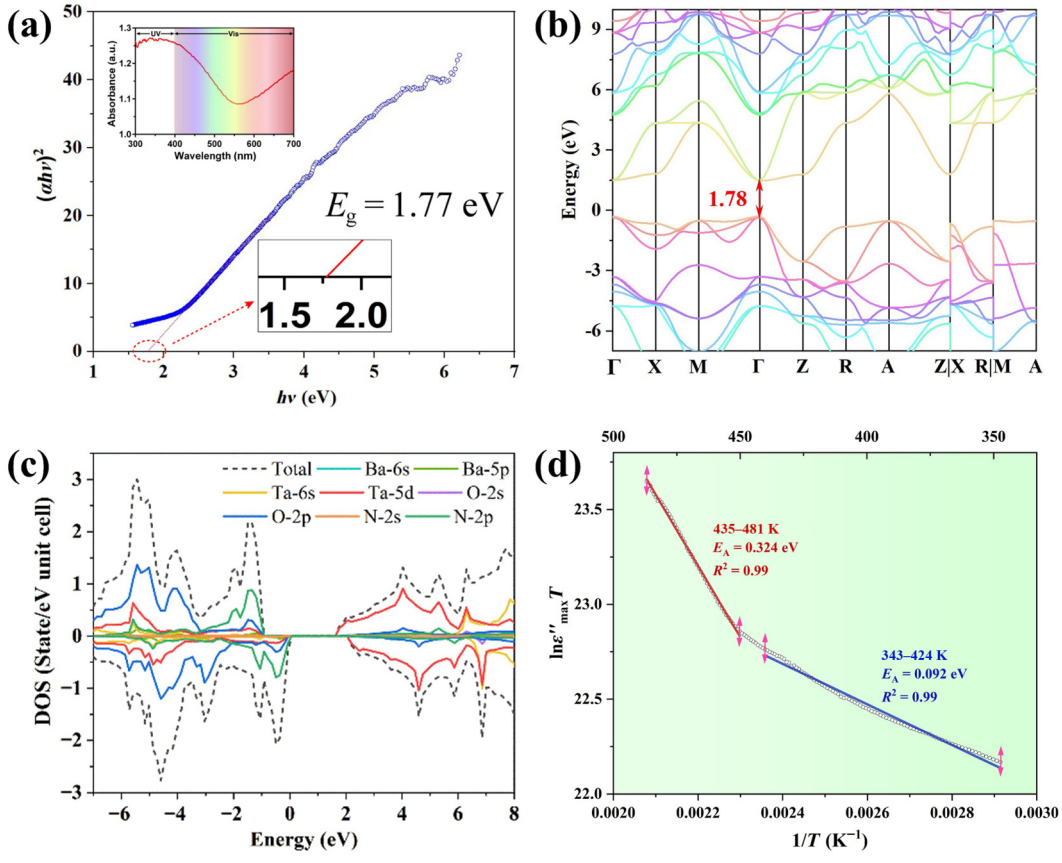

Fig. 6 Electronic structure and polarization characteristics of $BaTa(O,N)_3$: (a) UV-Vis diffuse reflectance spectroscopy and the Kubelka–Munk method for band gap determination (E_g represents the band gap value); (b) band structure and (c) density of states for $BaTaO_2N$; (d) activation energy for polaron hopping polarization.

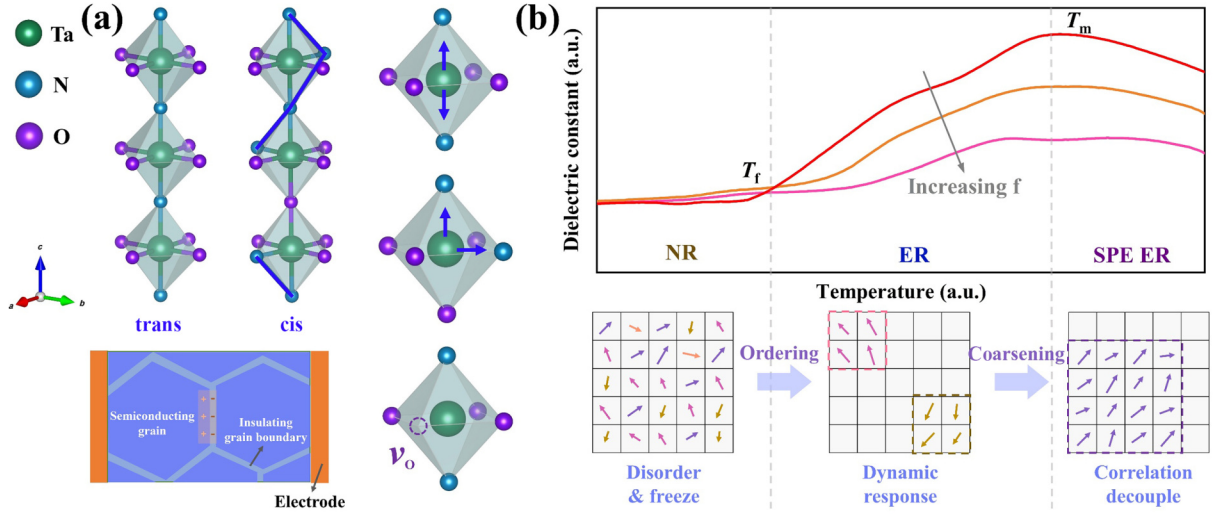

Fig. 7 Synergistic mechanisms of the collective permittivity: (a) *cis*/*trans* configurations and associated Ta^{5+} displacements, IBLC model, and oxygen vacancy; (b) thermally activated dielectric relaxation (the three temperature zones correspond to the polarization responses of the nonergodic relaxor NR, ergodic relaxor ER, and superparaelectric (SPE) ER).

nanoceramic bulks. This approach effectively overcomes the critical limitations of conventional sintering, which typically yields low-density samples with impurities, achieving a remarkable theoretical density of 96.7% and an oxynitride phase purity of 97.94 wt% with a homogeneous nanoscale microstructure and uniform elemental distribution. Dielectric measurements revealed a room-temperature dielectric constant of 2.1×10^5 at 100 Hz and a remarkable increase to 10^7 at 250 °C, surpassing previously reported values for both oxide and oxynitride dielectrics. Theoretical calculations and *in situ* TEM analysis confirmed that the large permittivity originates from three synergistic mechanisms: interface barrier layer capacitance, defect-mediated polarization (anion ordering-induced permanent dipoles and oxygen vacancies) and thermally activated reconfigurable polar nanoregions. This work not only demonstrates a scalable and versatile synthesis route for dense, compositionally complex oxynitride ceramics but also provides fundamental insights into defect engineering and polarization dynamics.

Acknowledgements

This work was supported by the Science and Technology Innovation Program of Hunan Province (Grant No. 2023RC3024) and the National Natural Science Foundation of China (Grant No. 51702361).

Availability of data and materials

The data that support the findings of this study are available from the corresponding author upon reasonable request.

Competing interests

The authors have no competing interests to declare that are relevant to the content of this article.

References

[1] Chen KH, Xiao JD, Hisatomi T, *et al.* Transition-metal (oxy)nitride photocatalysts for water splitting. *Chem Sci* 2023, **14**: 9248–9257.
[2] Hojamberdiev M, Vargas R, Zhang FX, *et al.* Perovskite $BaTaO_2N$: From materials synthesis to solar water splitting. *Adv Sci* 2023, **10**: 2305179.
[3] Masubuchi Y. Novel synthetic approaches and morphological design of perovskite-type oxynitrides in powder and ceramic form. *Prog Solid State Chem* 2024, **73**: 100440.
[4] Xiao JD, Nakabayashi M, Hisatomi T, *et al.* Sub-50 nm perovskite-type tantalum-based oxynitride single crystals with enhanced photoactivity for water splitting. *Nat Commun* 2023, **14**: 8030.
[5] Liu XC, Yan LJ, Li WP, *et al.* Enhancing the photocatalytic activity of $CaTaO_2N$ for overall water splitting through surface nitride ion enrichment. *ACS Catal* 2024, **14**: 10561–10567.
[6] Li D, Zeng L, Li B, *et al.* Rapid synthesis of dielectric tantalum-based oxynitrides. *Mater Des* 2020, **187**: 108416.
[7] Wang YB, Jie WJ, Yang C, *et al.* Colossal permittivity materials as superior dielectrics for diverse applications. *Adv Funct Mater* 2019, **29**: 1808118.
[8] Hosono A, Sun SK, Masubuchi Y, *et al.* Additive sintering and post-ammonolysis of dielectric $BaTaO_2N$ oxynitride perovskite. *J Eur Ceram Soc* 2016, **36**: 3341–3345.
[9] Hosono A, Masubuchi Y, Kikkawa S. Sintering behavior of dielectric $SrTaO_2N$ under high pressure of nitrogen. *Ceram Int* 2017, **43**: 2737–2742.
[10] Kikkawa S, Hosono A, Masubuchi Y. Remarkable effects of local structure in tantalum and niobium oxynitrides. *Prog Solid State Chem* 2018, **51**: 71–80.
[11] Castets A, Fina I, Guarín JR, *et al.* High-temperature synthesis and dielectric properties of LaTaON2. *Inorg Chem* 2021, **60**: 16484–16491.
[12] Masubuchi Y, Miyamoto D, Higuchi M. B_2O_3 as a new sintering additive for perovskite-type SrTaO2N oxynitride ceramics. *J Asian Ceram Soc* 2022, **10**: 158–164.
[13] Takeuchi H, Miyamoto D, Masubuchi Y, *et al.* Preparation of thick dense ceramic films of dielectric $BaTaO_2N$ through electrophoretic deposition. *Ceram Int* 2023, **49**: 21825–21829.
[14] Seol JW, Lee JS, Avdeev M, *et al.* Characterizations of structural, optical, and dielectric properties of oxynitride perovskites $ACa_{0.2}M_{0.8}O_{2.6}N_{0.4}$ (A= Sr, Ba; M = Nb, Ta). *Prog Solid State Chem* 2024, **73**: 100439.
[15] Dong BB, Cui JY, Gao YY, *et al.* Heterostructure of 1D Ta_3N_5 nanorod/$BaTaO_2N$ nanoparticle fabricated by a one-step ammonia thermal route for remarkably promoted solar hydrogen production. *Adv Mater* 2019, **31**: 1808185.
[16] Wang Z, Luo Y, Hisatomi T, *et al.* Sequential cocatalyst decoration on $BaTaO_2N$ towards highly-active *Z*-scheme water splitting. *Nat Commun* 2021, **12**: 1005.
[17] Chen KH, Xiao JD, Vequizo JJM, *et al.* Overall water splitting by a $SrTaO_2N$-based photocatalyst decorated with an Ir-promoted Ru-based cocatalyst. *J Am Chem Soc* 2023, **145**: 3839–3843.
[18] Yu JX, Shi L, Li RH, *et al.* Single-crystalline $LaTiO_2N$ nanosheets with regulated defects for photocatalytic overall water splitting under visible light up to 600 nm. *ACS Catal* 2024, **14**: 608–618.
[19] Zhang YR, Motohashi T, Masubuchi Y, *et al.* Sintering and dielectric properties of perovskite $SrTaO_2N$ ceramics. *J Eur Ceram Soc* 2012, **32**: 1269–1274.
[20] Zhang YR, Masubuchi Y, Motohashi T, *et al.* Hot isostatic press sintering and dielectric properties of $SrTaO_2N$ ceramics. *Ceram Int* 2013, **39**: 3377–3380.
[21] Shen ZJ, Zhao Z, Peng H, *et al.* Formation of tough interlocking microstructures in silicon nitride ceramics by dynamic ripening. *Nature* 2002, **417**: 266–269.
[22] Hosono A, Inoguchi M, Masubuchi Y, *et al.* Spark plasma sintering of dielectric $BaTaO_2N$ close to the melting point of the $BaCN_2$ additive. *J Eur Ceram Soc* 2020, **40**: 2317–2322.
[23] Li JS, Zeng L, Liu RJ, *et al.* Functional strontium tantalum oxynitride ceramics: Efficient synthesis, densification and dielectric performance. *J Inorg Mater* 2023, **38**: 885.
[24] Yang Y, Bi JQ, Qiao LJ, *et al.* Effect of grain size on mechanical properties and tribological behavior of size-tunable high entropy diboride ceramics obtained by two-step SPS sintering. *J Adv Ceram* 2024, **13**: 1835–1843.
[25] Yang MH, Oró-Solé J, Rodgers JA, *et al.* Anion order in perovskite oxynitrides. *Nat Chem* 2011, **3**: 47–52.
[26] Vonrüti N, Aschauer U. Anion order and spontaneous polarization in $LaTiO_2N$ oxynitride thin films. *Phys Rev Lett* 2018, **120**: 046001.
[27] Lan ZY, Vegge T, Castelli IE. Theoretical insight on anion ordering, strain, and doping engineering of the oxygen evolution reaction in $BaTaO_2N$. *Chem Mater* 2021, **33**: 3297–3303.
[28] Young SD, Chen JD, Sun WH, *et al.* Thermodynamic stability and anion ordering of perovskite oxynitrides. *Chem Mater* 2023, **35**: 5975–5987.
[29] Aagesen LK, Pitts SA, Harris BK, *et al.* Electrochemical grand potential-based phase-field simulation of electric field-assisted sintering. *Acta Mater* 2024, **275**: 120049.
[30] Ishii A, Yamanaka A, Yoshinaga M, *et al.* High-fidelity phase-field simulation of solid-state sintering enabled by Bayesian data assimilation using *in situ* electron tomography data. *Acta Mater* 2024, **278**: 120251.
[31] Wang ZJ, Meng YZ, Tang SL, *et al.* Simultaneous achievement of large electrocaloric effect and ultra-wide operating temperature range in $BaTiO_3$-based lead-free ceramic. *J Adv Ceram* 2024, **13**: 1234–1241.
[32] Dan YJ, Tang LP, Ning WZ, *et al.* Achieving enhanced energy storage performance and ultra-fast discharge time in tungsten–bronze ceramic. *J Adv Ceram* 2024, **13**: 1349–1358.
[33] Zhu ML, Liu K, Meng YZ, *et al.* Enhanced temperature stability of colossal-permittivity Ce-doped $SrTiO_3$ ceramics designed by defect engineering. *J Am Ceram Soc* 2025, **108**: 20365.
[34] Cai JH, Qi JL, Yang YY, *et al.* Colossal permittivity and ultralow dielectric loss in Nb-doped $SrTiO_3$ ceramics. *J Adv Ceram* 2023, **12**: 2247–2256.
[35] Cao ZZ, Zhao JJ, Fan JT, *et al.* Colossal permittivity of (Gd + Nb) co-doped TiO_2 ceramics induced by interface effects and defect cluster. *Ceram Int* 2021, **47**: 6711–6719.
[36] Jiang Z, Shi MY, Wang ZT, *et al.* Giant dielectric permittivity of Ca and Sb-co-doped TiO_2 ceramics. *J Mater Sci Mater Electron* 2022, **33**: 18389–18399.
[37] Wang ZT, Zhang L, Liu J, *et al.* Colossal permittivity characteristics and origin of (Sr,Sb) co-doped TiO_2 ceramics. *ECS J Solid State Sci Technol* 2022, **11**: 093002.
[38] Wang ZT, Li TY, Li JM, *et al.* A comparative study of microstructure and electrical properties of (Al,Nb) co-doped TiO_2 ceramics by different sintering methods. *Ceram Int* 2023, **49**: 18525–18533.
[39] Yang ZZ, Wang X, Zhang L, *et al.* Effect of limited current on ultrarapid densification and giant dielectric properties of flash sintering (La,Ta) co-doped TiO_2 ceramics. *J Mater Sci Mater Electron* 2024, **35**: 758.

[40] Wang B, Pu YP, Zhang L, *et al.* Novel $SrTiO_3$-based ceramics with colossal permittivity, low dielectric loss, and high insulation resistivity *via* defect engineering. *Ceram Int* 2022, **48**: 25484–25494.
[41] Xie HC, Pu YP, Shang YC, *et al.* High resistivity under colossal permittivity $SrTiO_3$ based ceramic via controlling ion diffusion. *Ceram Int* 2024, **50**: 12672–12677.
[42] Li KC, Hao H, Yao ZH, *et al.* Colossal permittivity and low dielectric loss in (Nb,Ga) co-doped $SrTiO_3$ ceramics sintered in nitrogen atmosphere. *Ceram Int* 2024, **50**: 8662–8668.
[43] Lu YC, Hsiang HI. Effects of A/B ratio on the dielectric properties and AC conductivity behaviors of La-doped $SrTiO_3$ with colossal permittivity. *J Alloys Compd* 2024, **1008**: 176558.
[44] Li LX, Xie JL, Wang ML, *et al.* Colossal permittivity (Nb,Mg) co-doped $BaTiO_3$ ceramics with excellent temperature stability and high insulation resistivity. *Ceram Int* 2021, **47**: 10072–10078.
[45] Zhang K, Li LX, Wang ML, *et al.* The self-compensation mechanism in barium titanate ceramics with colossal permittivity. *J Alloys Compd* 2021, **851**: 156856.
[46] Mo SY, Tang C, Zhang H, *et al.* Colossal permittivity and excellent temperature stability of $BaTiO_3$ based fine ceramics with controlled grain growth. *Ceram Int* 2024, **50**: 11980–11988.
[47] Fan JT, He G, Long Z, *et al.* High insulation resistivity and low dielectric loss in (Ta,Al)-codoped $BaTiO_3$ colossal permittivity materials. *J Am Ceram Soc* 2024, **107**: 4854–4863.
[48] Fan TT, Shi Q, Xiao WR, *et al.* Colossal permittivity with ultra-wide temperature stability in Bi + Ca co-doped $BaTiO_3$. *J Materiomics* 2025, **11**: 100877.
[49] Lee SY, Song JH, Oh J, *et al.* Enhanced colossal permittivity in mono-doped $BaTiO_3$ via particle hydroxylation-induced defect dipoles. *J Mater Chem A* 2025, **13**: 475–485.
[50] Zhang JH, Li ZX, Liu YQ, *et al.* Enhanced dielectric properties of CCTO ceramics doped by different halogen elements. *J Mater Sci Mater Electron* 2020, **31**: 8481–8488.
[51] Peng ZH, Wu D, Liang PF, *et al.* Grain boundary engineering that induces ultrahigh permittivity and decreased dielectric loss in $CdCu_3Ti_4O_{12}$ ceramics. *J Am Ceram Soc* 2020, **103**: 1230–1240.
[52] Boonlakhorn J, Prachamon J, Jumpatam J, *et al.* Dielectric characteristics of a (Cd^{2+}, F^-) co-doped $CaCu_3Ti_4O_{12}/CaTiO_3$ binary system improved with increased dielectric permittivity and decreased dielectric loss tangent. *Results Phys* 2022, **34**: 105275.
[53] Li K, Cong S, Bian L, *et al.* Simultaneous enhancement of piezoelectricity and temperature stability in $Pb(Ni_{1/3}Nb_{2/3})O_3$–$PbZrO_3$–$PbTiO_3$ piezoelectric ceramics via Sm-modification. *J Adv Ceram* 2024, **13**: 1578–1589.
[54] Li DX, Deng W, Shen ZY, *et al.* Aliovalent Sm-doping enables BNT-based realxor ferroelectric ceramics with > 90% energy efficiency. *J Adv Ceram* 2024, **13**: 2043–2050.
[55] Kim J, Qi YB, Kumar A, *et al.* Size-driven phase evolution in ultrathin relaxor films. *Nat Nanotechnol* 2025, **20**: 478–486.
[56] Fu J, Xie AW, Zuo RZ, *et al.* A highly polarizable concentrated dipole glass for ultrahigh energy storage. *Nat Commun* 2024, **15**: 7338.
[57] Yang YL, Liu ZY, Ren PR, *et al.* Modulation of phase boundary and domain structures to engineer strain properties in BNT-based ferroelectrics. *J Adv Ceram* 2024, **13**: 967–975.
[58] Yu JX, Huang J, Li RH, *et al.* Fluorine-expedited nitridation of layered perovskite Sr_2TiO_4 for visible-light-driven photocatalytic overall water splitting. *Nat Commun* 2025, **16**: 361.
[59] Huang Y, Lv F, Han S, *et al.* Piezoelectricity in half-Heusler narrow-bandgap semiconductors. *Science* 2025, **387**: 1187–1192.
[60] Cao RY, Yang QL, Deng HX, *et al.* Softening of the optical phonon by reduced interatomic bonding strength without depolarization. *Nature* 2024, **634**: 1080–1085.
[61] Han H, Voisin C, Guillemet-Fritsch S, *et al.* Origin of colossal permittivity in $BaTiO_3$ via broadband dielectric spectroscopy. *J Appl Phys* 2013, **113**: 024102.
[62] Yang X, Li D, Ren ZH, *et al.* Colossal dielectric performance of pure barium titanate ceramics consolidated by spark plasma sintering. *RSC Adv* 2016, **6**: 75422–75429.
[63] Wang J, Gao DD, Xie JY, *et al.* Polaron hopping induced giant room-temperature magnetodielectric effect in disordered rutile $NiNb_2O_6$. *Adv Funct Mater* 2021, **31**: 2108950.
[64] Xue KY, Wang ML, Du MK, *et al.* Synergistic modulation of $SrTiO_3$–TiO_2 colossal permittivity system by internal lattice defects and phase composition: Experimental and theoretical investigations. *Int J Hydrog Energy* 2024, **90**: 104–113.
[65] Luo BC, Feng W, Dai SW, *et al.* Stabilizing oxygen vacancies and promoting electrostrain in lead-free potassium niobate-based piezoelectrics over wide temperature ranges. *J Adv Ceram* 2024, **13**: 1965–1973.
[66] Dong W, Tian F, Ma Q, *et al.* High-performance colossal permittivity behaviour persists to ultralow temperature in Co+Ta co-doped SnO_2: A spin-defect mediated superstable large electronic moment of defect-dipole. *Acta Mater* 2021, **213**: 116965.